Range resolution and sampling frequency trade-off for GPS passive radar

ZHANG Zhuxian[1,2], ZHENG Yu[2], ZHENG Linhua[1,*], and ZHU Peidong[2]

1. College of Electronic Science, National University of Defense Technology, Changsha 410073, China;
2. College of Electronic Communication and Electrical Engineering, Changsha University, Changsha 410022, China

Abstract: In a global positioning system (GPS) passive radar, a high resolution requires a high sampling frequency, which increases the computational load. Balancing the computational load and the range resolution is challenging. This paper presents a method to trade off the range resolution and the computational load by experimentally determining the optimal sampling frequency through an analysis of multiple sets of GPS satellite data at different sampling frequencies. The test data are used to construct a range resolution-sampling frequency trade-off model using least-squares estimation. The theoretical analysis shows that the experimental data are the best fit using smoothing and nth-order derivative splines. Using field GPS C/A code signal-based GPS radar, the trade-off between the optimal sampling frequency is determined to be in the 20 461.25 –24 553.5 kHz range, which supports a resolution of 43–48 m. Compared with the conventional method, the CPU time is reduced by approximately 50%.

Keywords: global positioning system (GPS) radar, range resolution, sampling frequency, trade-off.

1. Introduction

GPS is widely used [1], and GPS-based remote sensing has been extensively studied in recent decades [2]. GPS radar is a type of passive radar that offers such advantages as not needing a specific radar transmitter, easy concealment, low cost, and strong resistance to electronic interference, and thus has been of great interest to the remote sensing community. GPS passive radar systems have been applied to monitoring sea surfaces [3,4], detecting vegetation coverage [5], and measuring changes in soil moisture [6] and snow thickness [7−9].

Resolution is an important factor in GPS passive

radars. Conventional imaging approaches based on the back-projection (BP) algorithm are limited by the signal bandwidth. Therefore, many researchers have used the high-bandwidth global navigation satellite system (GNSS) signal as source of opportunity to improve the range resolution [10−13]. However, increasing the bandwidth signal or implementing bandwidth synthesis is unable to solve the problem of aliasing of the multitarget reflection signals of a pseudo-random code chip. To address this issue, Zeng et al. [14] developed a method using the diff2 operator on the range compression signal to identify multiple objects using a single pseudo-random noise code chip. However, this method requires a high sampling rate, which increases the computational load and thus is a challenge in real-time GPS radar applications. Therefore, how to balance the range resolution and the computational load is worth examining. Few studies have examined this trade-off in the context of GNSS radars.

As discussed in previous works, computational load is a significant problem in real-time radar systems [15]. In active radar systems, numerous studies have investigated real-time radar imaging systems for different applications, such as real-time 3D radars, synthetic aperture radar (SAR) motion error models, and drone detection [16−18]. Several algorithms have also been developed for specific functions within radar systems. For example, a sparse passive radar imaging method was developed and verified in [19]. In [20], an algorithm was developed that provided an efficient framework to calculate the rough terrain clutter within 0.019 8 s when using an Intel Xeon CPU E5-2680 2.8-GHz supercomputer with 128 GB RAM [20]. Furthermore, Salehi-barzegar et al. [21] proposed the application of the nonuniform fast Fourier transform to the diffraction tomography image reconstruction method for 3D through-the-wall radar imaging. This approach requires more than 9 s of CPU time when using a 3.2-GHz AMD Quad-Core CPU with 48 GB

RAM. Wang et al. proposed a deep radar object detection network that can effectively detect objects in radio frequency (RF) images [22]. However, the data transmitted by the satellite are very large and require several hours to process. In addition, GNSS signals have a 100% duty cycle, and the algorithms [19−22] are based on the sparse characteristics of the signal. Thus they cannot be applied in GNSS radar systems. Nevertheless, a few studies have examined real-time GNSS radar systems. Hence, a breakthrough mathematical scheme is crucial for reducing the sampling frequency with low range resolution loss for GNSS real-time radar.

Unlike in previous works on the range resolution of GNSS radars, in this paper, the computational load is examined, following which a trade-off model is developed for optimising the range resolution and the sampling frequency for real-time imaging. The main contributions of this paper are summarised below.

(i) A range resolution –computational load trade-off model is constructed for real-time imaging.

(ii) The least-squares method is used to fit the model, and smoothing and polynomial functions are used to fit the experimental data.

(iii) The optimal sampling frequency for a GPS radar passive system is determined and verified for various scenarios.

The rest of the paper is organized as follows. The principle and geometrical model of GPS passive radar imaging are presented in Section 2. An adaptive search for the sampling frequency and resolution is described in Section 3. The reliability of the obtained results and scope for future improvements are discussed in Section 4. Section 5 presents the conclusions.

2. GPS passive radar imaging principle and geometrical model

The experiment in this work is based on bistatic radar [23,24]. In a GPS-SAR system (Fig. 1), the right and left antennas receive the direct and reflected satellite signals, respectively, and the data carried by these signals are used to image the reflection area [25].
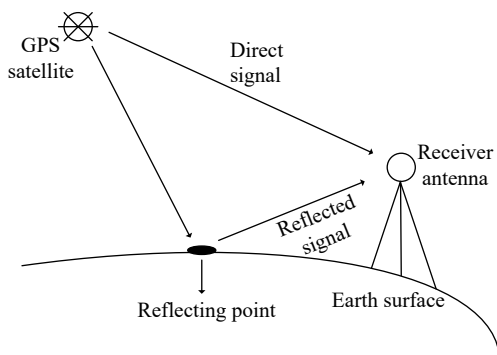

Fig. 1   GPS-SAR system model

The SAR imaging mode is used to obtain a pattern of the scattering area. The advantage of this mode is that the reflected and direct signals can be received simultaneously. That is, the GPS radar signals can be received using only a single receiver with two channels.

The main process in a GPS passive radar (Fig.2) comprises two steps: synchronisation and imaging. After receiving the direct and reflected signals, the receiver performs the synchronisation process, that is, the direct signal is correlated with the carrier signal at the corresponding frequency generated by the machine. Thereafter, carrier tracking and code tracking are performed. After synchronisation, the code delay, the carrier phase, and the navigation information of the signal are obtained. The BP algorithm is the core algorithm of the imaging process and is mainly used to match and filter the synchronised direct signal and the unsynchronised reflection signal to obtain the range-compressed signal [26−28]. Azimuth compression is the correlation operation performed on each sampling point along the azimuth domain resulting from the range compression.
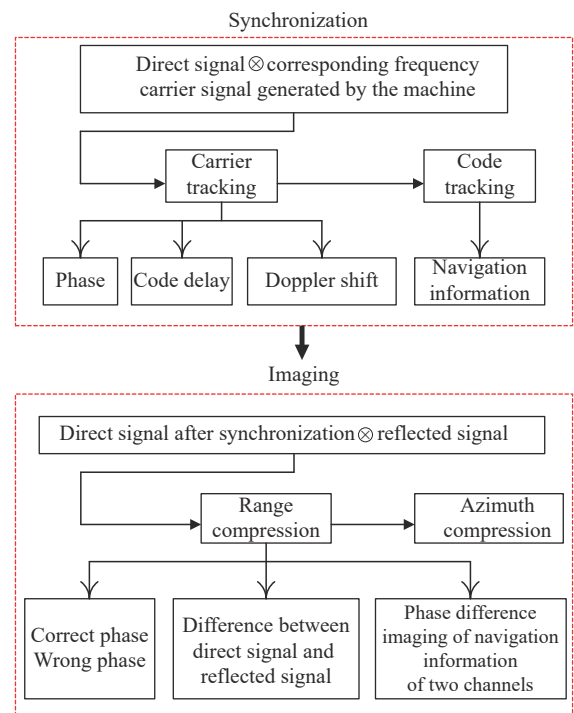

Fig. 2   Imaging model

The main synchronisation procedure is the convolution of the direct signal with the corresponding frequency carrier signal generated by the machine [29], where t_n represents the range domain, u represents the azimuth domain, τ represents the delay between reflected signal and direct signal, $C(t_n,\mu)$ denotes the synchronisation signal,

$S(t_n,\mu)$ is the direct signal, $S_{\text{ref}}(t_n,\mu)$ is the corresponding frequency carrier signal generated by the machine, and $\text{CF}_p[t_n - \tau(\mu)]$ is the cross-correlation function between the received signal and the local generated pseudo-code. D_p represents navigation data, ω_e represents Doppler frequency and the respective maximum value is 50 Hz, φ represents carrier phase.

$$C(t_n,\mu) = S(t_n,\mu) \otimes S_{\text{ref}}(t_n,\mu) =$$
$$\text{CF}_p[t_n - \tau(\mu)]D_p[t_n - \tau(\mu)] \cdot [j_e(\omega_e\mu t_n + \varphi(\mu)] \qquad (1)$$

The main imaging operation is to match and filter the direct and reflected signals after synchronisation, where $S_{rc}(t,\mu)$ denotes the imaging signal, $s(t,\mu,x,y)$ is the direct signal after synchronisation, and $S_{\text{sync}}(t_n,\mu)$ is the reflected signal after synchronisation. x, y represent the coordinate position of target relative to receiver, φ_{p2} represents the carrier phase of the matched filtered signal, $\omega_{d2} - \omega_{d1}$ represents Doppler frequency difference between reflected and direct signals.

$$S_{rc}(t,\mu) = s(t,\mu,x,y) \otimes S_{\text{sync}}(t_n,\mu) =$$
$$\text{CF}_p[t - (\tau_2(u,x,y) - \tau(\mu))] \cdot$$
$$\exp(j(\varphi_{p2}(\mu\mu x,y) + (\omega_{d2} - \omega_{d1})t_n)) \qquad (2)$$

3. Adaptive search for sampling frequency and resolution

In this section, the sampling frequency that can trade off range resolution and computational load is mathematically determined. Assuming M sampling points in each range direction, the calculation of the range correlation operation involves $M \times M$ multiplications and $M(M-1)$ additions, yielding a total of $M(2M-1)$ operations. Therefore, the diff2 operation entails $2M$ calculations. The recovery of the generated carrier phase requires M recovery factors and the calculation of M recovery processes. Therefore, $M(2M-1) + 4M$ calculations are performed for the range compression process. The computations performed for the GPS radar using the diff2-based range compression scheme are shown in Table 1.

Table 1 Computation in imaging processing

Imaging step	Times of multiplication	Times of addition/subtraction	Total
Range correlation operator	$M \times M$	$M(M-1)$	$M(2M-1)$
Secondary order differentiation operator	0	$2M$	$2M$
Generating reply factor in carrier phase recovery	0	M	M
Recover process in carrier phase recovery	0	M	M
Total operations	−	−	$M(2M-1) + 4M$

The results presented in Table 1 show that the computational time increases exponentially with the sampling frequency. The objective of this work is to determine the sampling frequency that balances range resolution and the computational time. Introducing the diff2 operator makes the resolution more sensitive to the sampling frequency [14]. That is, a small change in the sampling frequency may produce a large change in the resolution. Therefore, a model, called the resolution-sampling frequency model, is constructed to relate the resolution to the sampling frequency and then used to determine the optimal sampling frequency. The objective is to achieve a relatively high resolution at a relatively low computational load.

$$\begin{cases} R_{\text{range}} = af_{\text{sampling}}, \ f_{\text{sampling}} \leqslant O \\ R_{\text{range}} \approx b, \ f_{\text{sampling}} > O \end{cases} \qquad (3)$$

where R_{range} represents the range resolution, N_{sampling} represents the sampling frequency, f_{sampling} represents sampling frequency, O represents the optimal sampling frequency, and a and b are constants. The range resolution is proportional to the sampling frequency when the sampling frequency is less than or equal to O; otherwise, the range resolution has no effect on the sampling frequency. The resolution-sampling frequency model is analysed to find the optimal trade-off between the resolution and the computational load.

Fig. 3 illustrates the process for optimising the sampling frequency. First, an imaging experiment is performed to obtain the range resolution results at different sampling frequencies. Second, the test data are fitted. A better fit is obtained with a smoothing function than a polynomial function; hence, a smoothing function is used in the next step. The fitted resolution-sampling frequency curve is analysed to determine the optimal sampling frequency. The results are then verified by comparing them against dataset.

The imaging results show numerous bright, striped bars. The range resolution is calculated by using (4), where R_{range} represents the range resolution, N_{sampling} the number of sampling points, and W the number of imaged bright, striped bars. In this work, the imaging range signal has a main lobe width of 3 dB.
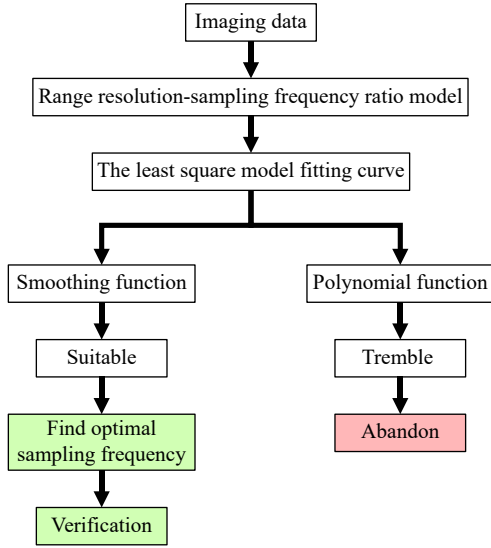
Fig. 3   Process of finding optimal sampling frequency

$$R_{\text{range}} = \frac{1 \times 3 \times 10^8}{N_{\text{sampling}}} \times W. \qquad (4)$$

Third, the resolution-sampling frequency curve is fit using the least-squares method. The curve-fitting tool in Matlab can be used to fit, both linearly and nonlinearly, various complex models [30]. As mentioned earlier, resolution increases with sampling frequency, but only up to a certain threshold, meaning that the resolution-sampling frequency curve is nonlinear. The two main nonlinear curve-fitting methods are the least-squares and spline interpolation methods. The least-squares method requires a curve to pass through every discrete test point, which is only practicable when extremely accurate function values are available; otherwise, a spline can be effectively constructed by interpolation. Because the accuracy of the experimental data is unknown, the spline interpolation method is used in this work.

The most widely used spline interpolation methods are the smoothing spline and the nth-order derivative spline. A variable p is considered in the smoothing spline method, presented in the next formula, to ensure that the fitted value is as close as possible to the experimental value [31]. However, the most suitable smoothing functions will be given through compromise [32]. The terms $[x_1, y_1]$ represent the data, ζ the error, and $p \in (0, \cdots, 1)$ the smoothing parameter.

$$F_{s1} = p \sum_{i=1}^{N} \left(\frac{y_i - f(x_i)}{\xi y_i} \right)^2 + (1-p) \int_{x_1}^{x_N} \left(f^{(m)}(t) \right)^2 \mathrm{d}t \qquad (5)$$

where F_{s1} represents the smoothing function.

The nth-order derivative spline formula is defined in segments. A third-derivative spline is considered here as an example. The spline curve $S_i(x)$ is defined in five segments, and its equation is given [33] as follows:

$$S_i(x) = p_1(x - x_i)^5 + p_2(x - x_i)^4 + p_3(x - x_i)^3 + p_4(x - x_i)^2 + p_5(x - x_i) + p_6, \quad i = 0, 1, \cdots, n-1. \qquad (6)$$

The spline algorithm is used to calculate the coefficients for each spline equation to yield a specific expression for the fitted curve.

4. Experimental study

Experimental data were collected at the Hong Kong Polytechnic University using the equipment shown in Fig. 4 [14], namely a GPS receiver, two antennas (to receive the direct and reflected signals), and a GPS receiver RF frontend. The right-side elliptically polarised direct antenna receives the direct signal, and the left-side elliptically polarised surveillance antenna receives the reflected signal. GPS-SAR was realised by circularly moving the surveillance antenna at a uniform velocity of approximately $1°/\text{s}$. The experimental data were obtained using a GPS C/A code signal with an L1 band.
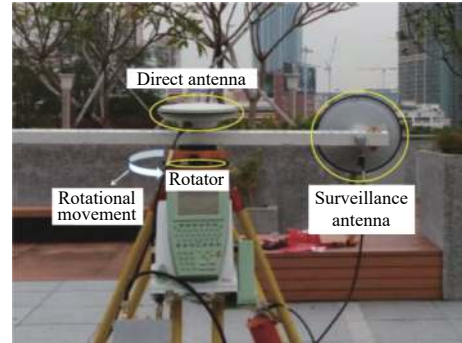
(a) Direct and surveillance antennas
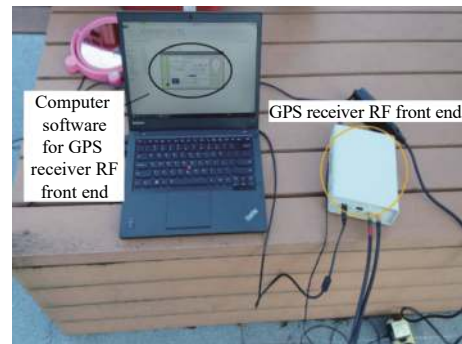
(b) GPS L1 C/A code signal receiver RF front end

Fig. 4   Experimental equipment [14]

The target object for detection, namely a reflection plate placed on a slope with no obstructions nearby, is shown in Fig. 5. Raw data were collected for 1 min. The experiment had two components: optimising the sampling frequency and verifying the result.
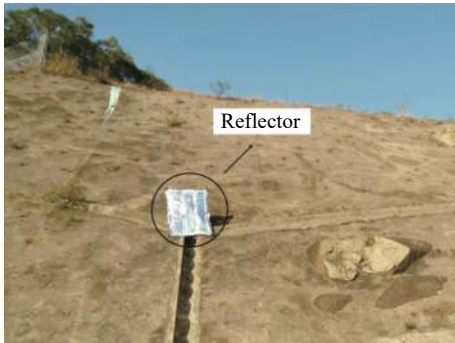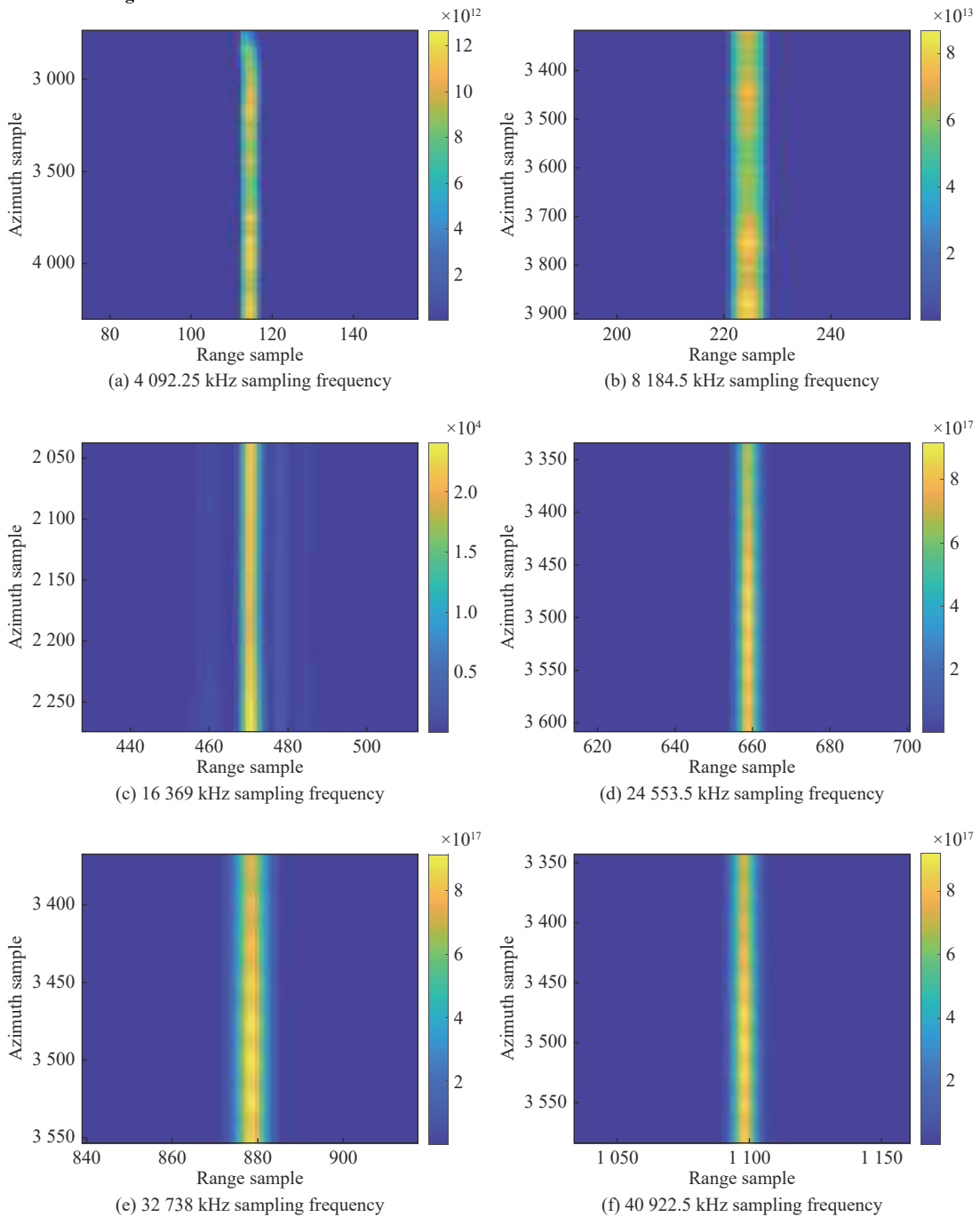
Fig. 5   Test scenario

The imaging algorithm was applied in a Matlab environment on a machine with a 3.2-GHz Intel Core(TM) i7-8 700 CPU and 32 GB RAM.

4.1   Determination of optimal sampling frequency

The first step in optimising the sampling frequency is imaging. Fig. 6 shows the range-compressed signal at different sampling frequencies obtained from Satellite 15 using the diff2 operator. The bright, striped bar in Fig. 6 is the most reflective component in the range sample.
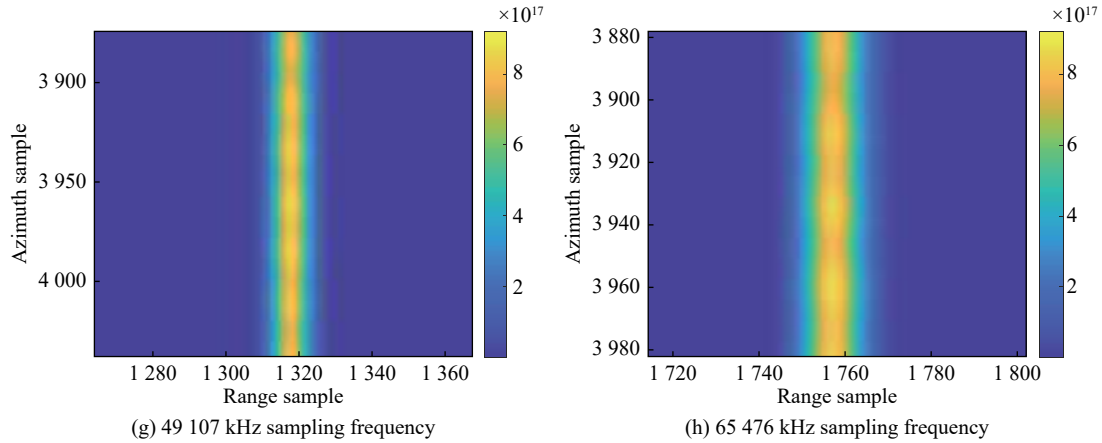

(a) 4 092.25 kHz sampling frequency

(b) 8 184.5 kHz sampling frequency

(c) 16 369 kHz sampling frequency

(d) 24 553.5 kHz sampling frequency

(e) 32 738 kHz sampling frequency

(f) 40 922.5 kHz sampling frequency

(g) 49 107 kHz sampling frequency   (h) 65 476 kHz sampling frequency

Fig. 6   Range compressed signal indifferent sampling frequency from Satellite 15

Table 2 summarises relationship between the sampling frequency and the resolution and shows that the optimal sampling frequency ranges from 16 369 kHz to 32 738 kHz. Although the optimal sampling frequency can also be estimated as 1 –2 times the sampling frequency of the front receiver, a mathematical analysis is performed to accurately determine the optimal sampling frequency.

Table 2   Range resolution results from Satellite 15

Sampling frequency/kHz	Number of samples	Resolution/m
4 092.25	4	293.24
8 184.50	6	219.93
16 369.00	4	73.31
24 553.50	4	48.87
32 738.00	6	54.98
40 922.50	6	43.98
49 107.00	7	42.76
65 476.00	10	45.82

Fig.7 shows the correlation between the resolution and the sampling frequency obtained using a fifth-order derivative spline. The black dots denote the experiment data, and the blue line is the fitting curve, the formula for which is given in the following:

$$S_i(x) = -2.052 \times 10^{-21}(x-x_i)^5 + 5.225 \times 10^{-16}(x-x_i)^4 -$$
$$5.104 \times 10^{-11}(x-x_i)^3 + 2.378 \times 10^{-6}(x-x_i)^2 -$$
$$0.052\,52(x-x_i) + 485.9, \quad i = 0, 1, \cdots, n-1. \quad (7)$$
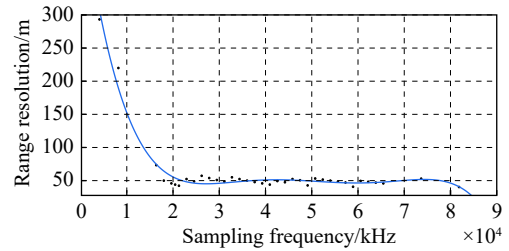

Fig. 7   Fifth-order derivative spline fitting curve from Satellite 15

The parameters of the fitting curve for the range resolution-sampling frequency model are as follows: coefficient of determination (R-square) = 0.973 9, root-mean-squared error (RMSE) = 8.591, and adjusted R-square = 0.969 6.

Fig. 8 shows the result obtained using a smoothing spline. The black dots denote the experimental data, and the blue line is the fitting curve, the formula for which is given in the following:

$$F_{s2} = p \sum_{i=1}^{N} \left(\frac{y_i - f(x_i)}{\xi y_i} \right) + (1+p) \int_{x_1}^{x_N} \left(f^{(m)}(t) \right)^2 dt,$$
$$p = 1.941\,010^{-9} \quad (8)$$

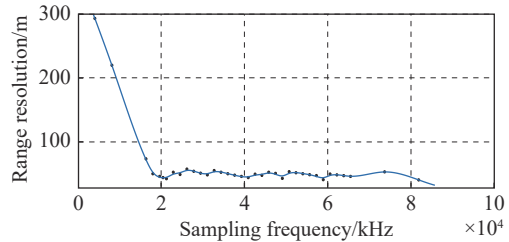where F_{s2} is the smoothing function from Satellite 15.

Fig. 8   Smoothing spline fitting curve from Satellite 15

The parameters for the fitted results are as follows: R-square = 0.995 5, RMSE = 3.951, and adjusted R-

square = 0.993 6.

The fifth-order derivative spline has more deviations than the smoothing spline does. Smoothing splines tend to be more suitable than nth-order derivative spines for theoretically analysing GPS-SAR data. Therefore, the smoothing spline fitting curve is used in the remainder of this work. The computational time for the range compression process is $M(2M − 1) + 4M$, that is, the number of computations is $M(2M − 1) + 4M$ times the sampling frequency.

Fig. 8 shows the optimal sampling frequency over the 8 184.5–24 553.5 kHz range. Next, by excluding the 0–2×10^9 kHz range, derivatives are calculated to determine the inflection point. The result in Fig. 9 indicates that 21 670 kHz is the optimal sampling frequency.
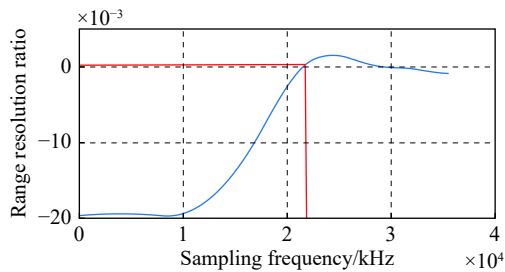

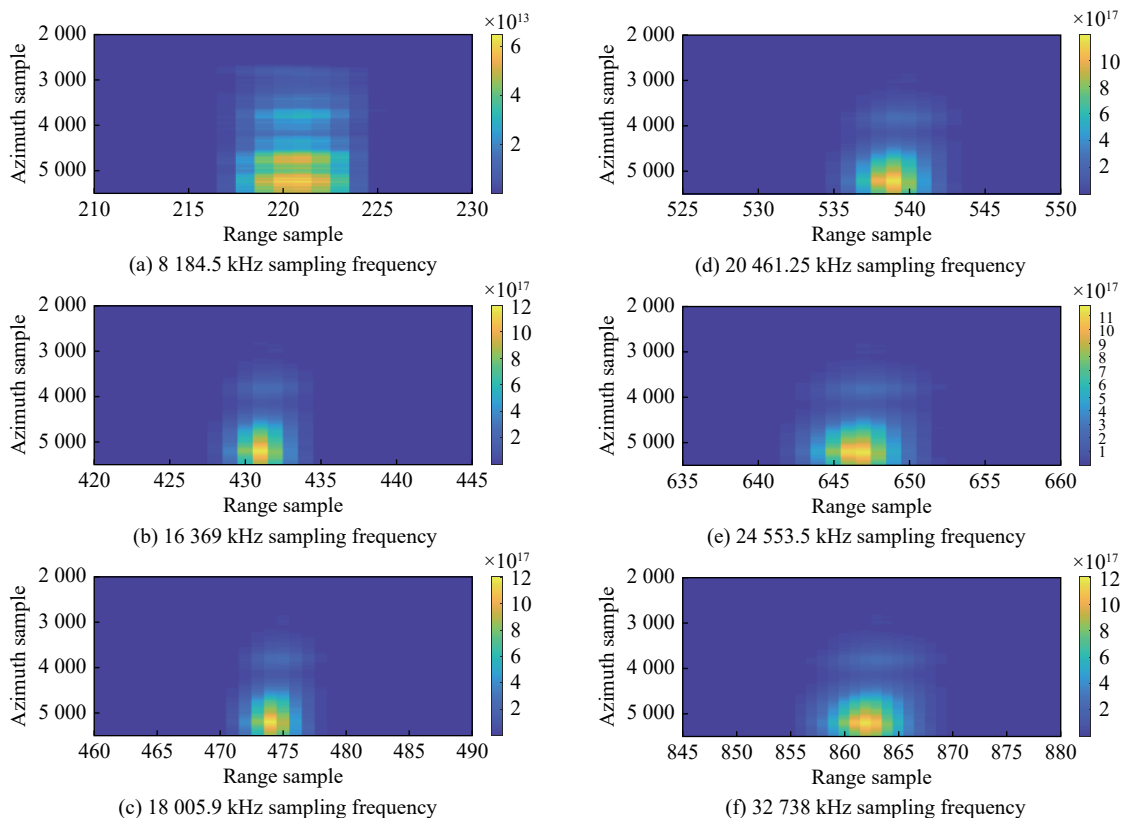Fig. 9   Differentiation result from Satellite 15

Compared with the traditional imaging approach, in which a sampling frequency of 32 738 kHz is used, the optimal sampling frequency determined in this work (21 670 kHz) eliminates nearly one third of the computations and requires only half the CPU time. Specifically, the CPU time is reduced by approximately 50% on a machine running a 3.2-GHz Intel Core(TM) i7-870 0 CPU and 32 GB RAM.

4.2   Verification of optimization result

To verify the optimisation, experimental data are obtained from Satellite 29. Fig. 10 shows the diffraction pattern results. The magnified image of the area around the brightest illuminated pixel are zoomed in Fig. 10. In Fig. 11, the abscissa range is the same as in Fig. 10, but the difference in the sampling rate changes the corresponding coordinates and resolution of the sampling points.

The relationship between the sampling frequency and the resolution for the data obtained from Satellite 29 is presented in Table 3, which indicates that the optimal sampling frequency ranges from 20 461.25 kHz to 24 553.5 kHz. Thus, the data obtained from Satellite 29 verify the optimal sampling frequency derived from the fitting curve.

(a) 8 184.5 kHz sampling frequency

(b) 16 369 kHz sampling frequency

(c) 18 005.9 kHz sampling frequency

(d) 20 461.25 kHz sampling frequency

(e) 24 553.5 kHz sampling frequency

(f) 32 738 kHz sampling frequency

Fig. 10   Diffraction pattern results from Satellite 29

(a) 8 184.5 kHz sampling frequency

(b) 16 396 kHz sampling frequency

(c) 18 005.9 kHz sampling frequency

(d) 20 461.25 kHz sampling frequency

(e) 24 553.5 kHz sampling frequency
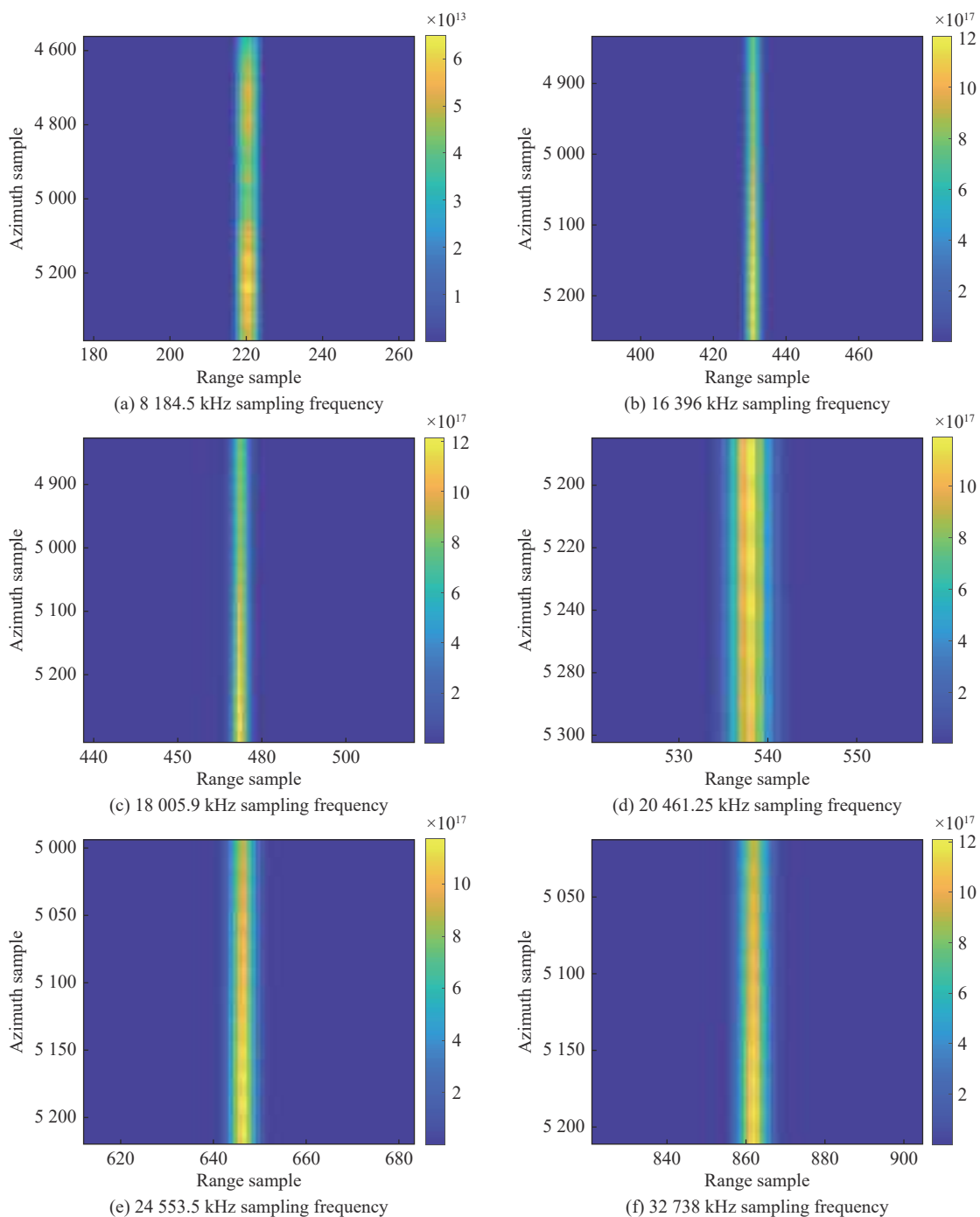
(f) 32 738 kHz sampling frequency

Fig. 11   Imaging results from Satellite 29

Table 3   Ranging result comparison with 3 dB main lobe width from Satellite 29

Sampling frequency/kHz	Number of samples	Resolution/m
8 184.50	5	183.27
16 369.00	4	73.31
18 005.90	3	49.98
20 461.25	3	43.98
24 553.50	4	48.87
32 738.00	5	45.82

5. Conclusions and future work

In this paper, the trade-off between the sampling frequency and resolution obtained using the diff2 operator was investigated. The relationship between the resolution and sampling frequency is determined using least-squares estimation and a smoothing function. Using field GPS C/A code signal data, the optimal sampling frequency is determined to be in the 20 461.25–24 553.5 kHz range, which supports a range resolution of 43–48 m. Compared

with the conventional method, the CPU time is reduced by nearly 50%. The experimental results show that the proposed method can be applied to various types of data obtained from different GPS satellite signals.

In future studies, the proposed adaptive method will be applied to realize other objectives in different environments. For real-time imaging, because the receiver movement in SAR imaging is slow (approximately $1°/s$), the sampling frequency can be further decreased with azimuth compression, which in turn will decrease the computational load. Compressive sensing, commonly used to improve system efficiency, might be suitable for the azimuth compression of GPS passive radar systems.

References

[1] FRNTI P, MARIESCU-ISTODOR R. Averaging GPS segments competition 2019. Pattern Recognition, 2021, 112: 107730.

[2] ZHUANG X S, WANG L. Moving target imaging method for passive radar applicable to non-cooperative illumination source. Systems Engineering and Electronics, 2015, 37(3): 560–565. (in Chinese)

[3] BALASUNRAMANIAM R, RUF C. Characterization of rain impact on L-band GNSS-R ocean surface measurements. Remote Sensing of Environment, 2020, 239: 111607.

[4] GEREMIA-NIEVINSKI F, HOBIGER T, HAAS R, et al. SNR-based GNSS reflectometry for coastal sea-level altimetry: results from the first IAG inter-comparison campaign. Journal of Geodesy, 2020, 94(8): 70.

[5] PAN Y L, REN C, LIANG Y J, et al. Inversion of surface vegetation water content based on GNSS-IR and MODIS data fusion. Satellite Navigation, 2020, 1(1): 21.

[6] YUEH S H, SHAH R, CHAUBELL M J, et al. A semiempirical modeling of soil moisture, vegetation, and surface roughness impact on CYGNSS reflectometry data. IEEE Trans. on Geoscience and Remote Sensing, 2020. DOI: 10.1109/TGRS.2020.3035989.

[7] ZHANG Z Y, GUO F, ZHANG X H. Triple-frequency multi-GNSS reflectometry snow depth retrieval by using clustering and normalization algorithm to compensate terrain variation. GPS Solutions, 2020, 24(2): 52.

[8] MUNOZMARTIN J F, PEREZ A, CAMPS A, et al. Snow and ice thickness retrievals using GNSS-R: preliminary results of the MOSAiC experiment. Remote Sensing, 2020, 12(24): 4038.

[9] STEINER L, MEINDL M, MARTY C, et al. Impact of GPS processing on the estimation of snow water equivalent using refracted GPS signals. IEEE Trans. on Geoscience and Remote Sensing, 2020, 58(1): 123–135.

[10] CAMPS A, MUNOZ-MARTIN J F. Analytical computation of the spatial resolution in GNSS-R and experimental validation at L1 and L5. Remote Sensing, 2020, 12(23): 3910.

[11] ZHENG Y, YANG Y, CHEN W. A novel range compression algorithm for resolution enhancement in GNSS-SARs. Sensors, 2017, 17(7): 1496.

[12] CARTWRIGHT J, BANKS C J, SROKOSZ M. Improved GNSS-R bi-static altimetry and independent digital elevation models of Greenland and Antarctica from TechDemoSat-1. The Cryosphere, 2020, 14(6): 1909–1917.

[13] MA H, ANTONIOU M, PASTINA D, et al. Maritime moving target indication using passive GNSS-Based bistatic radar. IEEE Trans. on Aerospace and Electronic Systems, 2018, 54(1): 115–130.

[14] ZHENG Y, YANG Y, CHEN W. New imaging algorithm for range resolution improvement in passive Global Navigation Satellite System-based synthetic aperture radar. IET Radar, Sonar & Navigation, 2019, 13(12): 2166–2173.

[15] LONG T, ZENG T, HU C, et al. High resolution radar real-time signal and information processing. China Communications, 2019, 16(2): 105–133.

[16] TZADOK A, VALDES-GARCIA A, PEPELJUGOSKI P, et al. AI-driven event recognition with a real-time 3D 60-GHz radar system. Proc. of the IEEE/MTT-S International Microwave Symposium, 2020: 795–798.

[17] WANG H, ZENG Z, JIANG M, et al. Study on motion compensation method for W-band UAV MISAR real-time imaging. Proc. of the 21st International Radar Symposium, 2020: 143–147.

[18] DEMIR B, ERGUNAY S, NURLU G, et al. Real-time high-resolution omnidirectional imaging platform for drone detection and tracking. Journal of Real-Time Image Processing, 2020, 17: 1625–1635.

[19] BI H, BI G A, ZHANG B C, et al. From theory to application:real-time sparse SAR imaging. IEEE Trans. on Geoscience and Remote Sensing, 2020, 58(4): 2928–2936.

[20] TAJDINI M M, MORGENTHALER A W, RAPPAPORT C M. Multiview synthetic aperture ground-penetrating radar detection in rough terrain environment: a real-time 3-D forward model. IEEE Trans. on Geoscience and Remote Sensing, 2020, 58(5): 3400–3410.

[21] SALEHI-BARZEGAR A, CHELDAVI A, NAYYERI V, et al. A fast diffraction tomography algorithm for 3-D through-the-wall radar imaging using nonuniform fast fourier transform. IEEE Geoscience and Remote Sensing Letters, 2020, 19: 3504805.

[22] WANG Y Z, JIANG Z Y, LI Y D, et al. RODNet: a real-time radar object detection network cross-supervised by camera-radar fused object 3D localization. IEEE Journal of Selected Topics in Signal Processing, 2021, 15(4): 954−967.

[23] ZHOU X, WANG P, CHEN J, et al. A modified radon fourier transform for GNSS-Based bistatic radar target detection. IEEE Geoscience and Remote Sensing Letters, 2020, 19: 3501805.

[24] WANG S, BAO Q L. Single target tracking for noncooperative bistatic radar with unknown signal illumination. Signal Processing, 2021, 183: 107991.

[25] ZHENG Y, YANG Y, CHEN W. Object detectability enhancement under weak signals for passive GNSS-based SAR. 2019, 13(8): 1549−1557.

[26] SOMMER A. Backprojection autofocus of large ships with arbitrary motion for synthetic aperture radar. Berlin: University of Hanover, 2020.

[27] REN K, BURKHOLDER R J. A 3-D novel fast back projection imaging algorithm for stratified media based on near-field monostatic and bistatic SAR. IEEE Trans. on Antennas and Propagation, 2020, 69(4): 2326−2335.

[28] GAIBEL A, BOAG A. Back projection imaging of moving objects. IEEE Trans. on Antennas and Propagation, 2020. DOI: 1-1.10.1109/TAP.2020.3045500.

[29] ZENG Z F. Passive bistatic sar with GNSS transmitter and a stationary receiver. Britain: University of Birmingham, 2013.

[30] TAKANE Y, YOUNG F W, LEEUW J D. Nonmetric individual differences multidimensional scaling: an alternating least squares method with optimal scaling features. Psychometrika, 1977, 42(1): 7–67.

[31] QIU S, LI X M, HUANG Y D, et al. New algorithm of response curve for fitting HDR image. International Journal of Pattern Recognition and Artificial Intelligence, 2020, 34(1): 2054001.

[32] ZHANG Y, WANG R, LI S Z, et al. Temperature sensor denoising algorithm based on curve fitting and compound kalman filtering. Sensors, 2020, 20(7): 1959.

[33] WANG J, LU Y, YE L, et al. Efficient analysis-suitable T-spline fitting for freeform surface reconstruction and intelligent sampling. Precision Engineering, 2020, 66: 417–428.

Biographies

ZHANG Zhuxian was born in 1984. She received her M.S. degree in telecommunication from Melbourne University in 2009. She is now a Ph.D. candidate in National University of Defense Technology. Her main research in GNSS passive radar sensing include static and dynamic object detection.
E-mail: zxzhang@ccsu.edu.cn

ZHENG Yu was born in 1989. He received his B.E. degree and M.S. degree from Xiangtan University, China and University of Alberta, Canada in 2012 and 2014, respectively. In 2015, he joined the Department of Land Surveying and Geo-informatics, Hong Kong Polytechnic University as a Ph.D. student. He received his Ph.D. degree in 2018. Now he is a lecturer in the College of Electronic Communication and Electrical Engineering, Changsha University. His major research interests including environmental sensing using GNSS signals as source of opportunity and indoor location and surveillance using commercial devices.
E-mail: y_zheng170@sina.com

ZHENG Linhua was born in 1961. He received his Ph.D. degree from the College of Electronic Science and Engineering, National University of Defense Technology, Changsha, China. Currently he is a full professor with the same institution. He has published eight monographs and textbooks and over 100 technical papers. His research interests are wireless communication system, satellite communication, and radar signal processing.
E-mail: lhzheng131@sohu.com

ZHU Peidong was born in 1971. He received his Ph.D. degree in the College of Computer Science and Technology, National University of Defense Technology, Changsha, China in 1999. After that, he has been a faculty member in the same institution from lecturer to full professor. He was a visiting chair professor in Saint Xavier University from 2008 to 2009. Now he is a full professor and departmental head for the College of Electronic Communication and Electrical Engineering, Changsha University, Changsha, China. His main research interests are wireless communication networks and security assessment for radar network.
E-mail: pdzhu@nudt.edu.cn